PAPER

Experimental investigation of geodesic acoustic modes on JET using Doppler backscattering

IOP Publishing | International Atomic Energy Agency Nuclear Fusion

Nucl. Fusion **56** (2016) 106026 (10pp) doi:10.1088/0029-5515/56/10/106026

Experimental investigation of geodesic acoustic modes on JET using Doppler backscattering

C. Silva[1], J.C. Hillesheim[2], C. Hidalgo[3], E. Belonohy[4], E. Delabie[5], L. Gil[1], C.F. Maggi[2], L. Meneses[1], E. Solano[3], M. Tsalas[6] and JET Contributors[a]

EUROfusion Consortium, JET, Culham Science Centre, Abingdon, OX14 3DB, UK
[1] Instituto de Plasmas e Fusão Nuclear, Instituto Superior Técnico, Universidade de Lisboa, Lisbon, Portugal
[2] CCFE, Culham Science Centre, Abingdon, OX14 3DB, UK
[3] Laboratorio Nacional de Fusión, CIEMAT, 28040 Madrid, Spain
[4] Max-Planck-Institut fur Plasmaphysik, Boltzmannstr. 2, D-85748 Garching, Germany
[5] Oak Ridge National Laboratory, Oak Ridge, TN 37831-6169, USA
[6] FOM Inst. DIFFER, Nieuwegein, Netherlands

E-mail: csilva@ipfn.tecnico.ulisboa.pt

Received 2 February 2016, revised 24 June 2016
Accepted for publication 14 July 2016
Published 19 August 2016

Abstract

Geodesic acoustic modes (GAMs) have been investigated in JET ohmic discharges using mainly Doppler backscattering. Characteristics and scaling properties of the GAM are studied. Time and spatial resolved measurements of the perpendicular velocity indicate that GAMs are located in a narrow layer at the edge density gradient region with amplitude corresponding to about 50% of the mean local perpendicular velocity. GAMs on JET appear to be regulated by the turbulence drive rather than by their damping rate. It is also shown that the GAM amplitude is ~20% larger in deuterium than in hydrogen plasmas.

Keywords: edge turbulence, GAMs, Doppler backscattering

(Some figures may appear in colour only in the online journal)

1. Introduction

Spontaneously generated large-scale sheared flows such as zonal flows (ZFs) have been recognized to play an important role in the regulation of turbulent transport [1, 2]. Because of their small radial structure, the $E \times B$ shearing rate due to ZFs can be important before and during the L–H transition when the mean shear flow is modest (e.g. [1–4]).

Two major branches of ZFs are expected in magnetically confined toroidal plasmas: the near zero low frequency ZF and the oscillatory flows termed geodesic acoustic mode (GAM). The GAM oscillations are expected to have a $n = 0$, $m = 0$ electric potential structure, coupled by toroidal effects with a $n = 0$, $m = 1$ pressure perturbation [5]. More recently, a $n = 0$, $m = 2$ magnetic perturbation caused by the GAM has also been predicted by theory [6] and observed experimentally (e.g. [7]). The GAM has a finite radial structure with a wavelength of several ion Larmor radii, $k_r\rho_i < 1$, where ρ_i is the ion gyroradius and k_r the radial wavenumber. GAMs are predicted to oscillate with a frequency $f_{GAM} = Fc_s/(2\pi R)$, where $c_s = \sqrt{[(T_e + T_i)/m_i]}$ is the ion sound speed, R is the major radius, m_i the ion mass and T_e and T_i are the electron and ion temperature respectively. F is a coefficient of order unity, which depends on parameters such as safety factor and elongation [8–10]. As a result of the radial variation of the temperature, the GAM frequency is expected to depend on radius, having a so-called continuum structure. More recent theoretical works predict that the mode frequency remains constant over a large radial extent due to finite Larmor radius effects [11, 12]. The eigenmodes are predicted to have discrete frequencies and an Airy function structure. With respect to experimental observations, some authors report discrete eigenmodes with a fixed frequency over some finite radial range over which c_s may vary substantially (e.g. [13–15]); others observe a smooth dependence of the mode frequency on local conditions

[a] See the appendix of [54].

at each radius (e.g. [13, 16, 17]). On DIII-D [13] and FT-2 [16] both regimes are observed in the same experiment. The physics difference between the two regimes was suggested to be related with whether finite ion Larmor radius effects are important [13]. Although GAMs are in general strongly damped in the core plasma, they have been observed in the core region of the JIPPT-IIU tokamak in low-density ohmic plasmas with $T_e/T_i \gg 1$ exhibiting a very wide spectrum ($\Delta f/f \sim 50\%$) [17, 18] as in this case the Landau damping is predicted to be rather small [18, 19].

There are two factors that determine the magnitude of the GAM: its drive and damping. The drive is thought to be due to nonlinear interactions with turbulence while the mode undergoes ion Landau damping that strongly depends on the safety factor ($\gamma \propto \exp[-q^2]$). GAMs are also weakly damped by ion collisions ($\gamma \propto \nu_{ii}$, where ν_{ii} is the ion collision rate). This means that the GAM is strongly damped in the core and may exist towards the edge where the safety factor is large. The GAM is generally most intense in the edge density gradient region. The inner radial extent is dictated by the q profile and by collisional damping (disappears at high densities). GAMs are not typically observed in H-mode but are nearly always present in ohmic and L-mode plasmas. It has been also found that GAMs can be excited by a population of fast ions, EGAMs (e.g. [20]). The controlled excitation of EGAMs in the presence of turbulence could lead to important studies of turbulent transport control [20].

A large number of experimental observations on the identification of the GAM key physics properties have been obtained in the last decade [13–38]. In particular, experimental measurements of GAMs have shown characteristics consistent with the theoretical predictions. It has become clear that an important role is played by the GAM in many phenomena, particularly as a saturation mechanism for turbulence. GAMs are the most experimentally diagnosable turbulence saturation mechanism mainly as a consequence of their well defined frequency, allowing the GAM to be easily distinguished experimentally from both low-frequency ZFs and equilibrium flows.

This contribution focuses on the characterization of GAMs in the edge plasma of JET ohmic discharges using mainly Doppler backscattering. Coherent oscillations consistent with the GAM theoretical predictions are identified and characterized. In addition, the dependence of GAM amplitude on the driving and damping mechanisms are investigated.

2. Experiment and diagnostic setup

2.1. Description of the experiment

Results presented in this paper were obtained during an experiment in JET aiming at assessing the possible connection between properties of large scale flows (e.g. GAMs) and isotope physics trying to contribute to the understanding of the isotopic effect. The influence of isotope mass on the GAM amplitude has been studied recently in different devices [39–41] showing a systematic increase in the GAM amplitude during the transition from hydrogen to deuterium dominated plasmas. Consequently, understanding GAMs may yield important implications for the dynamics of the L–H transition. The initial experimental plan aimed at characterizing GAMs and local turbulence in hydrogen and deuterium plasmas when approaching the L–H transition. However, due to limitations in the auxiliary input power available that prevented the H-mode to be achieved, the objective of the experiment was focused mainly in the GAM characterization in ohmic hydrogen plasmas.

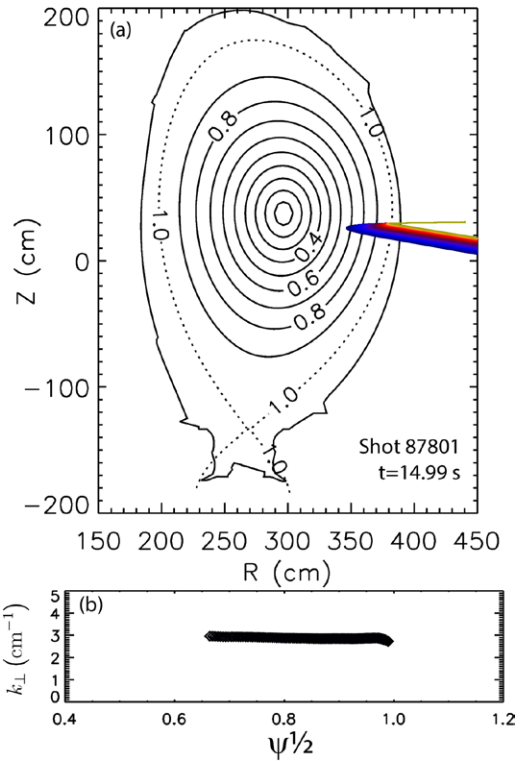

Figure 1. DBS ray tracing results for all the 165 probing frequencies (from 74.125 to 93.805 GHz) launched horizontally, overlayed on the EFIT equilibrium for pulse #87801 (*a*), together with the estimated perpendicular wavenumber (*b*).

The importance of critical aspects, such as the safety factor and collisionality in determining the GAM amplitude have been investigated under controlled plasma conditions in a dedicated experiment. The safety factor was varied by changing the plasma current in the range $1.5 < I_p < 2.75$ MA, with the magnetic field maintained constant resulting in a safety factor variation of $3.1 < q_{95} < 5.8$. A series of ohmic discharges were carried out in hydrogen, within a single day of JET plasma operation, where the plasma current was varied from pulse to pulse and within each discharge two or three density steps were performed. Steady state periods of 1.5–2 s are obtained for each density step allowing for a detailed plasma characterization. All discharges were performed in the vertical target (VT) configuration (plasmas with both divertor strike-points on the VTs, see figure 1) with an elongation of 1.7 and a toroidal magnetic field of $B_T = 3$ T. The main plasma parameters are shown in table 1.

2.2. Measurement technique and signal analysis

Doppler backscattering (DBS) is a microwave diagnostic for density fluctuation measurements that measures the radially

Table 1. Plasma parameters that were varied during a series of ohmic discharges at constant $B_T = 3$ T in hydrogen.

Pulse	I_p (MA)	Line-averaged density (10^{19} m^{-3})
87805	1.5	1.5–2.5
87804	1.75	1.5–2.6
87801	2.0	1.5–2.4–3.2
87803	2.25	1.6–2.7–3.6
87802	2.5	1.6–2.8–3.6
87808	2.75	2.8–3.9

localized propagation velocity and fluctuation level of intermediate wavenumber turbulent structures [42]. This diagnostic has contributed extensively to the characterization of coherent oscillations such as the GAM. Motion of the density turbulence near the cutoff layer induces a Doppler frequency shift (f_D) in the backscattered signal given by $f_D = u_\perp k_\perp/2\pi$, where $u_\perp = \nu_{E\times B} + \nu_{phase}$ is the perpendicular velocity of the turbulence moving in the plasma (e.g. [42]) and $k_\perp$ is the perpendicular wavenumber. For the VT configuration the JET correlation reflectometer [43, 44] works for DBS as a deliberate oblique angle between the launched beam and the normal to the plasma cutoff layer is created (see figure 1(*a*)) [45]. The scattering wavenumber of the density fluctuations is determined via ray tracing [46]. For the data presented here the typical probed $k_\perp$ is ~3 cm^{-1} across the entire radial region scanned by the DBS diagnostic (see figure 1(*b*)).

The Doppler frequency is obtained from the complex amplitude spectrum of the reflectometer in-phase ($I = A\cos\varphi$) and quadrature ($Q = A\sin\varphi$) signals. The instantaneous phase is obtained from $\varphi(t) = \tan^{-1}[Q(t)/I(t)]$ and the signal amplitude from $A(t) = [I^2(t) + Q^2(t)]^{1/2}$. Two data analysis techniques are typically used to derive the Doppler shift from the I and Q reflectometer signals (e.g. [14]): (i) sliding FFT method where the weighted mean of the complex amplitude signal is estimated and then Fourier analysed again to give the spectrum of the perpendicular velocity; (ii) phase derivative method to obtain the instantaneous Doppler shift directly from the rate of change of the reflectometer phase signal. The phase derivative method has an improved time resolution (original sampling period, 0.5 μs) over the sliding FFT method.

Figure 2 shows an example of the frequency power spectra of the amplitude and phase derivative signals. GAMs appear as a distinct peak in dφ/dt frequency spectra around 10 kHz, but not in the amplitude signal. As illustrated, the GAM amplitude is up to one order magnitude larger than the background fluctuations, although with a modest spectral power associated; the spectral power within the GAM peak is below 1% of the total signal power.

The results of the sliding FFT and phase derivative methods are compared in figure 3. For the sliding FFT method a 64 points window is applied to the complex signal with a step of 32 points and therefore the Nyquist frequency is limited to 62.5 kHz. As shown in figure 3, a good agreement (within 10%) is found between the two approaches. The GAM amplitude is then obtained integrating the Doppler shift power spectrum over the GAM peak for each probing frequency

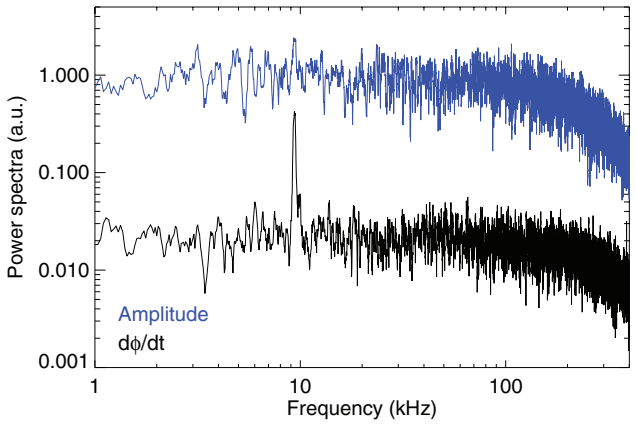

Figure 2. Frequency power spectra of the amplitude and phase derivative signals for discharge #87808.

step. Results presented in this paper correspond to the peak-to-peak GAM amplitude obtained with the phase derivative method. For convenience, the GAM amplitude may also be estimated by the rms of the phase derivative signal bandpass filtered around the GAM frequency. The GAM rms value is typically one third of the GAM peak-to-peak amplitude.

The JET correlation reflectometer consists of two X-mode fast frequency hopping channels launched from the LFS midplane designed for normal incidence. Each channel can be pre-programmed with a specified launch frequency pattern, which is repeated continuously throughout the discharge, allowing a radial scan of the measurement location. For the data presented here, channel 1 (master) was set to an 11 point frequency sweep (from 74.6 to 92.6 GHz), while channel 2 (slave) had a 15 point frequency sweep of 2 ms duration around each master frequency. The full frequency sweep takes 330 ms and at $B_T = 3$ T allows probing densities typically from 0.7 to 3×10^{19} m^{-3}. The measurement location was obtained using density profiles from the profile reflectometer diagnostic [47]. The value of the magnetic field was selected to allow for DBS measurements in the edge region of the plasma, where GAMs are typically observed.

3. GAM identification and location

In this section GAMs are identified using DBS and magnetic coils signals and their location and amplitude are determined. Figure 4 shows the temporal evolution of the line-averaged density (a) together with the spectrogram of a high-field-side (HFS) magnetic coil signal (b) for an ohmic discharge with three density steps where the GAM peak at ~10 kHz is clearly seen around the intermediate density step. GAMs are typically observed in magnetic signals mainly at the HFS. The present set of magnetic coils at JET does not allow a robust identification of the poloidal and toroidal structure of the modes. However, the poloidal structure of the GAM magnetic component was explored in similar discharges (e.g. 86849) when more magnetic coils were operational and a $m = 2$ mode structure has been identified, in agreement with theoretical predictions [6] and previous experimental observations (e.g. [7]).

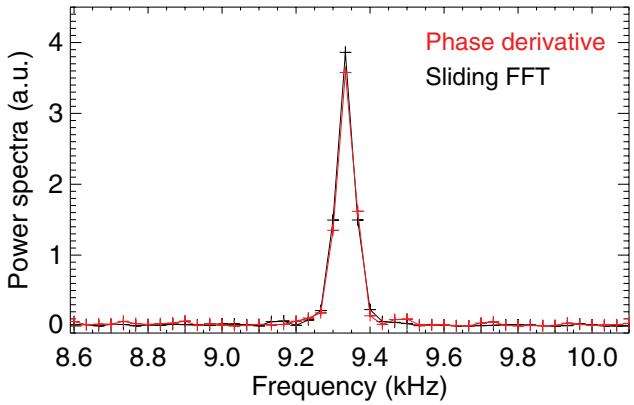

Figure 3. Power spectra of the Doppler shift estimated by the phase derivative and sliding FFT methods for a reflectometer master signal step.

The GAM frequency is observed to depend on the line-averaged density. The solid line shown in the spectrogram corresponds to the calculated GAM frequency using the local T_e given by three consecutive electron cyclotron emission (ECE) channels (assuming $F = 1$ and $T_i = T_e$). The electron temperature radial profile at $t = 15$ s is shown in figure 4(*c*) together with the location of the three ECE channels used in figure 4(*b*). Experimental measurements of the ion temperature were not available for this experiment but in discharges with similar conditions it was found that at the edge $T_e \approx T_i$ [48]. As illustrated, the observed GAM frequency follows very closely the local electron temperature ($f_{GAM} \propto \sqrt{T_e}$). Interestingly, the GAM frequency peak in the magnetic coils signals is very narrow, suggesting either a constant frequency across mode or a very localized mode. The GAM peak width is below 0.3 kHz (full-width at half-maximum of the peak) that would imply a temperature variation below 15 eV across the GAM existence region, assuming that the frequency is determined locally.

Figure 5 shows the temporal evolution of the line-averaged density and reflectometry master probing frequency, together with the spectrogram of the master signal phase derivative. As illustrated, the frequency spectrum of the phase derivative is also sharply peaked at the GAM frequency. GAMs are not continuously observed in figure 5 as they do not exist across the entire radial region scanned by the DBS diagnostic.

Figure 6(*a*) shows the electron density radial profile, obtained with the profile reflectometry system, for two periods of the discharge #87808 ($t = 12$ and 15 s) with different line-averaged densities. The location of the master probing frequencies, obtained from the profile reflectometer, is also shown (symbols). The horizontal error bars represent the uncertainty in the density profile (standard deviation of the probing frequency location during each master frequency step). Figures 6(*b*) and (*c*) present the GAM amplitude and frequency respectively, while figure 6(*d*) shows the radial profile of the mean perpendicular velocity. These DBS measurements were performed over a 1 s period (roughly three full frequency sweeps). As illustrated, GAMs are generally most intense in the edge density gradient region near the pedestal top with a radial extension of about 3 cm, coinciding with the location of the

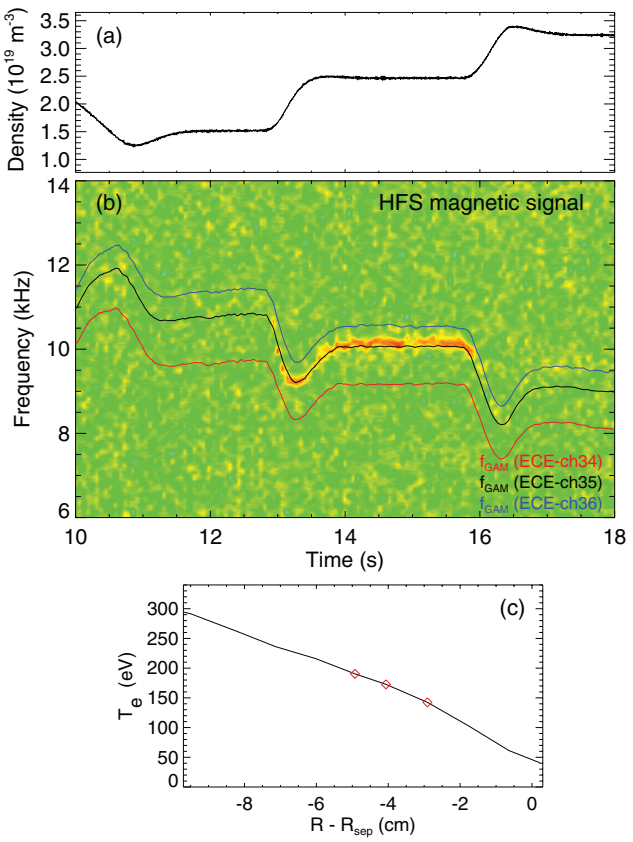

Figure 4. Temporal evolution of the line-averaged density (*a*) and spectrogram of a HFS magnetic coil signal for discharge #87801 (*b*). The solid lines overlayed in the spectrogram indicates the GAM frequency estimated using the local T_e given by three consecutive ECE channels. (*c*) Electron temperature radial profile at $t = 15$ s together with the location of the three ECE channels used in (*b*).

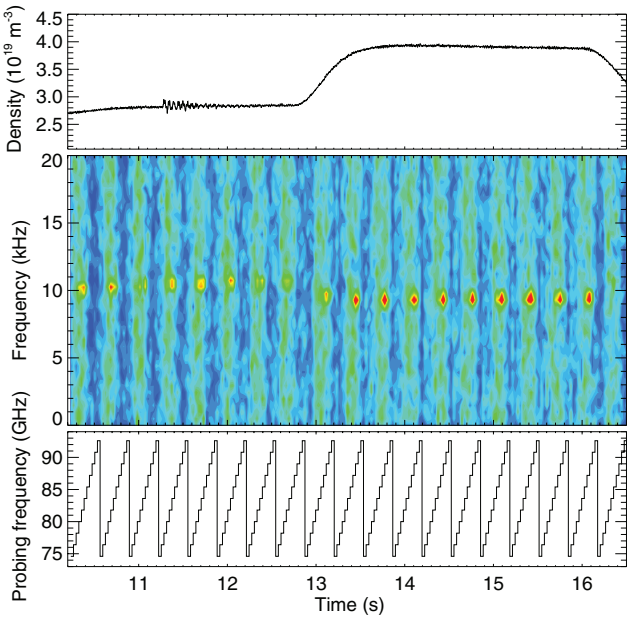

Figure 5. Temporal evolution of the line-averaged density, spectrogram of the reflectometry master signal phase derivative and master probing frequency for discharge #87808.

radial electric field (E_r) well. The GAM amplitude is reduced before the separatrix and is undetectable in the scrape-off layer

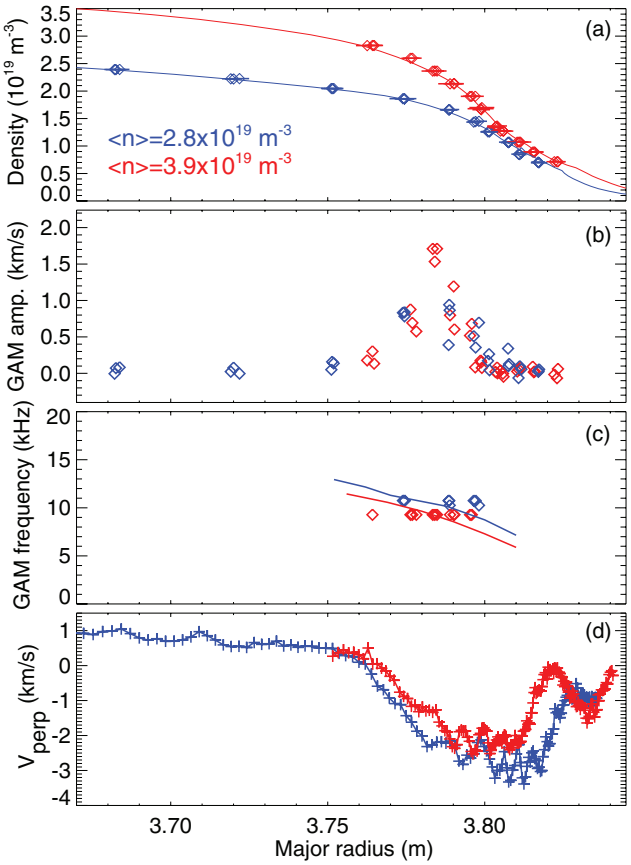

Figure 6. Radial profiles of density (*a*), GAM amplitude (*b*) and frequency (*c*) and mean perpendicular velocity (*d*) for two discharge periods ($t = 12$ and 15 s) with different line-averaged density (#87808).

as typically observed in different devices [13–16, 22–24]. However, the existence of GAMs in the core plasma cannot be excluded as this region is not accessible to the DBS diagnostic at $B_T = 3$ T except at low densities. The GAM has a constant frequency with radius, not varying with the local temperature (the calculated continuum GAM frequency using the local T_e is indicated by the solid line in figure 6(*c*)) that is consistent with descriptions of the GAM as a radial eigenmode. The GAM $E_r \times B$ flow velocity is up to ~1.5 km s^{-1}, corresponding to about 50% of the local mean perpendicular velocity. The fine-scale spatial structures observed in the edge E_r well have been shown to be consistent with stationary ZFs [49]. Comparing profiles in the two discharge periods with different line-averaged density it is found that GAMs are stronger at high density where the E_r well is narrower. Results reported here with respect to the GAM radial location and the observation of a locked frequency are similar to observations in other devices such as DIII-D [13, 22] or AUG [14].

The intermittent character of GAMs has been reported in different devices [13, 14, 23, 24]. Figure 7 shows the temporal evolution of the perpendicular velocity derived from the DBS master signal bandpass filtered around GAM frequency ($f_{GAM} \pm 3$ kHz). As illustrated, the perpendicular velocity at the GAM frequency is not constant in time varying from periods where the GAM practically vanishes to peak-to-peak amplitudes in the order of 3 km s^{-1}. In spite of this intermittency,

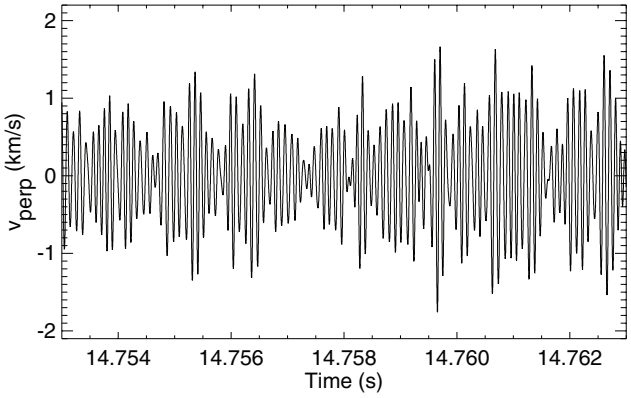

Figure 7. Temporal evolution of the perpendicular velocity bandpass filtered around f_{GAM} for discharge #87802.

the GAM oscillation has a relatively long correlation time; the GAM auto-correlation time is typically around 5 ms (corresponding to about 50 GAM periods), that is significantly larger than that of the ambient turbulence (in the order of a few μs). The evolution of the GAM amplitude at different time scales has been evaluated to determine the uncertainty resulting from the GAM intermittency. Taking as reference the duration of the master frequency step (30 ms), the variation of the GAM amplitude from step-to-step and within each step has been studied. For a window length of 6 ms, the standard deviation of the GAM amplitude within a frequency step is in the order of 0.15 km s^{-1}. Between master steps with the same probing frequency (for plasma steady-state conditions) the standard deviation is down to 0.1 km s^{-1}. This latter value will be considered the uncertainty of the GAM amplitude estimation.

The analysis presented in this section was performed with the DBS master signals. The use of the slave signal is apparently advantageous as it allows a finer radial resolution of the measurements (there are 15 slave frequency steps within each master one). It is however important to note that the intermittency in the GAM amplitude has to be taken into account when using the slave signals. As illustrated in figure 7, the GAM amplitude is highly intermittent in a time scale of a few ms. As the duration of the slave frequency step is only 2 ms, the GAM intermittency leads to a larger scatter in the estimate of the GAM amplitude. Analysis performed with the slave signal provides therefore a higher spatial resolution at a cost of a reduced statistics.

4. GAM radial structure

It is predicted that the GAM pattern in the radial direction is oscillatory and complex (finite radial wavenumber) exhibiting a structure on the scale of 10–50 ρ_i that evolves on the turbulence time scales. The two reflectometer channels sample simultaneously different radial plasma locations hinting the possibility to infer the radial structure of the GAM. During each master frequency step the measurement location of the slave signal is radially scanned. The correlation between master and slave signals may therefore be used to determine the GAM radial structure. The diagnostic settings used in this experiment are however not ideal for correlation analysis

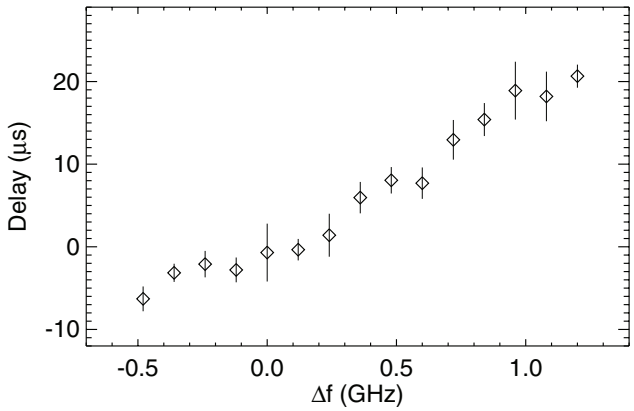

Figure 8. Delay at maximum cross-correlation (between the master and slave signals) for the different slave frequency steps for discharge #87808. Δf indicates the probing frequency difference between the master and slave signals.

as each slave frequency step is only 2 ms long, not allowing therefore for a robust statistics and consequently leading to large uncertainties in the determination of the GAM radial structure.

The cross-correlation between the master and slave signals as a function of the time lag has been determined for different slave frequency steps within the same master step and the delay at the maximum cross-correlation estimated. Figure 8 shows the delay at maximum cross-correlation as a function of the probing frequency difference between the master and slave signals. A master frequency probing the plasma near the GAM maximum amplitude has been chosen. A delay of about ~25 μs is observed across the 15 slave frequencies that corresponds roughly to one fourth of the GAM period. Taking into account that the frequency scan used covers about 0.6 cm radially, a radial wavelength in the order of 2.4 cm is estimated ($k_r \sim 2.6\,\mathrm{cm}^{-1}$). We conclude that the GAM radial wavelength is roughly of the dimension of GAM existence region. This corresponds to approximately 30 times the ion Larmor radius. The radial wavenumber obtained is in agreement with a mesoscale radial structure theoretically predicted for the GAM radial structure, $k_r\rho_i < 1$. Data presented in figure 8 is consistent with the mode propagating radially outwards as often observed in experiments (e.g. [7, 13]), but contrary to the reported in FT-2 [40].

The GAM radial correlation length can also be investigated from the analysis of the correlation between the master and slave signals. As mentioned before, during each master frequency step the measurement location of the slave signal is radially scanned covering about 0.6 cm radially. This means that the radial correlation of the GAM cannot be estimated across its full existence region. For the data presented in figure 8 no significant changes of the maximum correlation value are observed when the measurement location of the slave signal is radially scanned. We conclude therefore that the radial correlation length for the GAM is significantly larger than 0.6 cm. This is larger than the typical turbulence correlation length as observed in different devices [7, 13, 16].

The $E \times B$ shearing rate associated with the GAM can now be estimated from the calculated GAM amplitude and radial

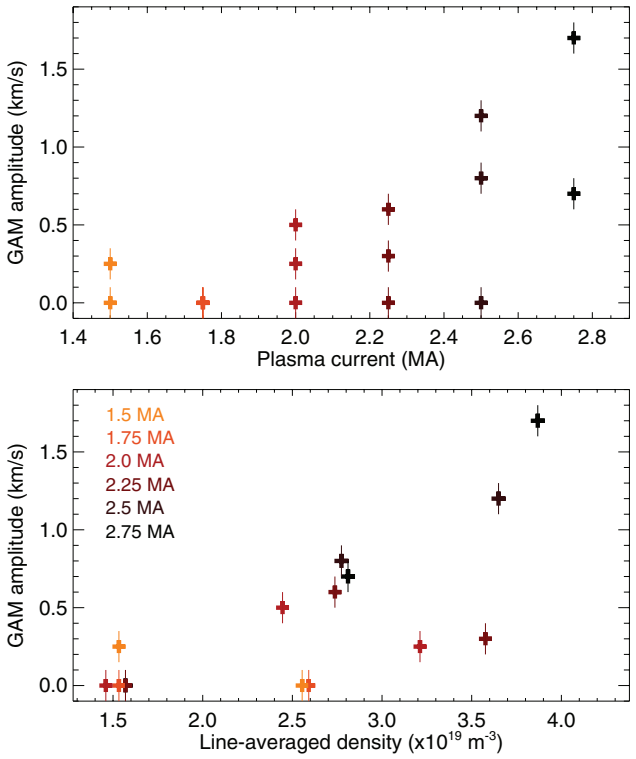

Figure 9. Dependence of the GAM amplitude on the plasma current and line-averaged density.

wavenumber, $\omega_{E\times B} \sim k_r A_{\mathrm{GAM,rms}}$. For the analyzed JET ohmic discharges the GAM rms value is typically below 0.5 km s^{-1} and therefore the GAM shearing rate is up to ~1.3×10^5 s^{-1}, that is comparable to the turbulence decorrelation time (~4×10^5 s^{-1}) derived from the turbulence auto-correlation time. The values for the GAM radial structure and shearing rate are consistent with a previous estimate on JET using reciprocating probe data in limiter plasmas ($k_r \approx 1.4$–$1.8\,\mathrm{cm}^{-1}$, $\omega_{E\times B} \sim 1.5 - 2 \times 10^5$ s^{-1}) [24]. The GAM shear rate is also comparable to the equilibrium $E \times B$ shearing rate (~2×10^5 s^{-1}, see figure 6(*d*)). Note however that the GAM shear rate is expected to be less effective than the equilibrium one since the shearing effect is reduced as the frequency increases [50].

5. GAM damping and driving mechanisms

As described in the introduction the magnitude of the GAM is determined by the drive and damping mechanism. In this section we start by analysing the scaling of the GAM amplitude with the damping terms and then investigate the GAM turbulence drive. A series of six ohmic discharges where performed in hydrogen for different values of plasma current ($1.5 < I_p < 2.75$ MA) and line-averaged density (varied from 1.5 to 3.9×10^{19} m^{-3}), see table 1.

Figure 9 shows the GAM amplitude as a function of the main plasma parameters varied during the experiment: plasma current and line-averaged density. The values shown correspond to the maximum of the GAM amplitude across the radial region scanned by the DBS. The DBS measurements were averaged over steady-state discharge periods within each

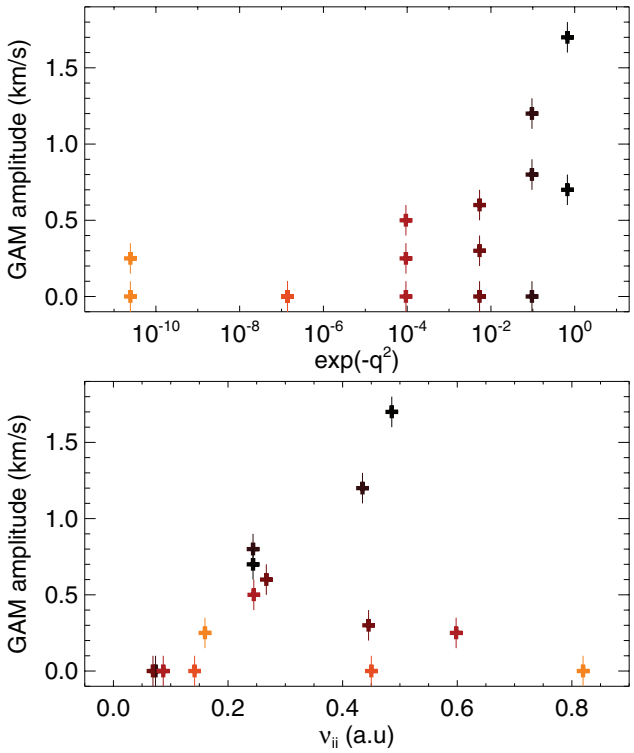

Figure 10. Dependence of the GAM amplitude on the predicted collisionless and collisional damping rates.

density step (typically 1.5 s). Note that no GAMs are observed for some density steps corresponding to data with zero amplitude. The different values for each I_p in figure 9 correspond to the different density steps within the discharge. Results demonstrate that the plasma current has a strong effect on the GAM amplitude, with the GAM increasing rapidly at high I_p, contrary to the theoretical expectations and experimental results in several devices [14, 22]. The dependence on the discharge density is more complex but at least for the higher I_p discharges an increase of the GAM amplitude with density is observed.

We will investigate now the dependence of the GAM amplitude on the expected GAM damping rates for the collisionless ($\gamma \propto \exp[-q^2]$) and collisional ($\gamma \propto \nu_{ii}$) cases (see figure 10). The safety factor was varied by changing the plasma current and the collisionality by modifying the plasma current and density. The GAM amplitude is observed to decrease with q_{95}, in contradiction with the anticipated for the collisionless damping that predicts increased damping at low q. Although experiments in other devices generally report an increase of the GAM amplitude with q, AUG data for divertor configuration with a similar elongation used in our experiment ($\kappa = 1.7$) also shows a small decrease of the GAM amplitude with the local q [14]. Contrary to theoretical predictions for collisional damping, no decrease of the GAM amplitude with ν_{ii} is observed. Consequently, the GAM amplitude on JET does not appear to be regulated by its linear damping mechanisms alone.

Our attention is now turned to the study of the turbulence drive as GAMs are driven by turbulence. Figure 11 shows the dependence of the GAM amplitude on the plasma electron pressure at the position of the maximum GAM amplitude. The GAM amplitude increases sharply above a certain value of

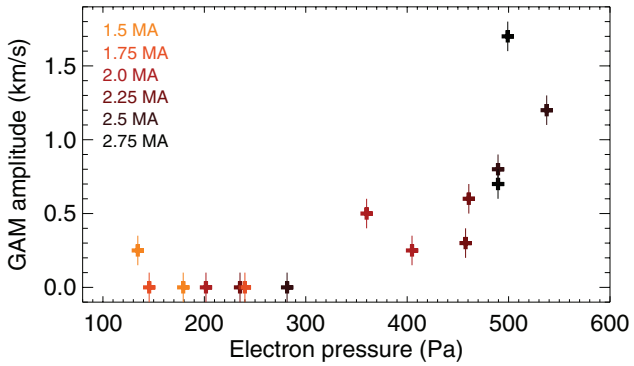

Figure 11. Dependence of the GAM amplitude on the plasma electron pressure at the position of the maximum GAM amplitude.

local electron pressure indicating that a minimum pressure or pressure gradient is apparently required to drive GAMs, supporting a turbulence drive mechanism.

Figure 12 shows the frequency power spectra of the DBS signals for different values of plasma current and line-averaged density. For low turbulence levels the amplitude of the backscattered signal is proportional to the density fluctuations. The amplitude of the density fluctuations increases with plasma current (by about ~40% from $I_p = 1.5$ to 2.75 MA) and with line-averaged density (by a factor of ~2.3 from $\langle n \rangle = 1.6$ to 3.6×10^{19} m^{-3}) as observed with the GAM amplitude dependence. This result suggests that GAMs on JET ohmic plasmas are regulated by the turbulence drive.

To better understand the turbulence drive the behaviour of the edge profiles and respective inverse scale lengths (the inverse gradient scale lengths are the drive terms for drift-wave type turbulence) are now investigated. Figure 13 shows the density and temperature equilibrium profiles and their respective inverse scale length ($1/L_{n,T}$) for different discharge densities. Electron temperature profiles measurements are from the ECE diagnostic (averaged over 100 ms) and density from the profile reflectometer. For the lowest discharge density, $1/L_{n,T}$ is small as there is no edge pedestal and GAMs are not detected. Then, the inverse temperature, density and electron pressure scale lengths increase with line-averaged density in the GAM region (indicated by the shaded area). Note also that the inner most radial limit for the GAM detection corresponds roughly to the location where $1/L_{n,T}$ is observed to increase significantly. In summary, for our dataset of ohmic discharges it is generally observed that the density fluctuation levels, as well as the edge plasma density and temperature inverse scale lengths, increase with plasma current and line-averaged density, concurrent with the enhancement of the GAM amplitude. Our results suggest that the edge pressure gradient plays an important role in determining the GAM amplitude.

It is also important to note that the GAM drive is due to nonlinear interactions with turbulence through processes such as the Reynolds stress. The latter is determined not only by the turbulence level but also by the phasing between the fluctuating fields that is not available. Although there are no particular reasons to believe that the underlying linear instability changes for our experimental conditions we cannot unequivocally demonstrate the GAM turbulence drive.

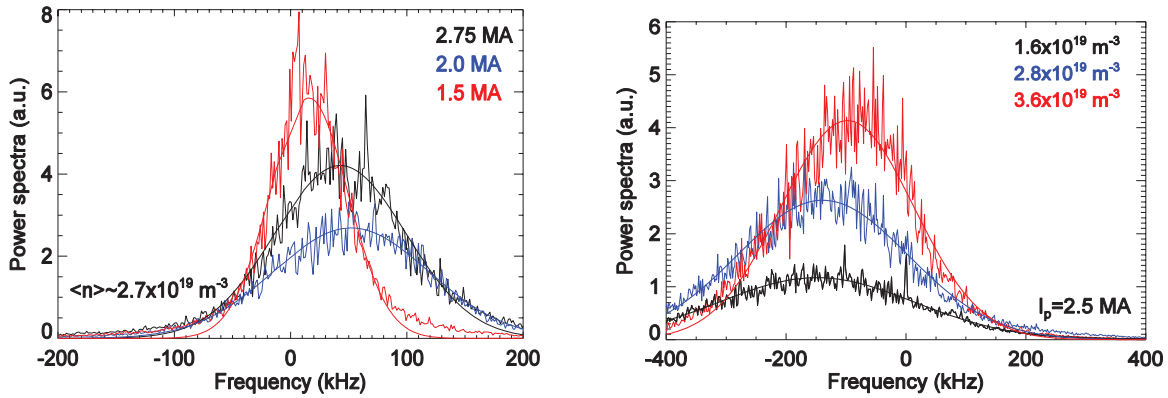

Figure 12. Frequency power spectra of the DBS signals for different values of plasma current (left) and line-averaged density (right). In the latter case distinct probing frequencies were used for the different line-averaged density values so that the measuring location is roughly the same. The launched power at different frequencies was considered by normalizing to the amplitude of the signals without plasmas.

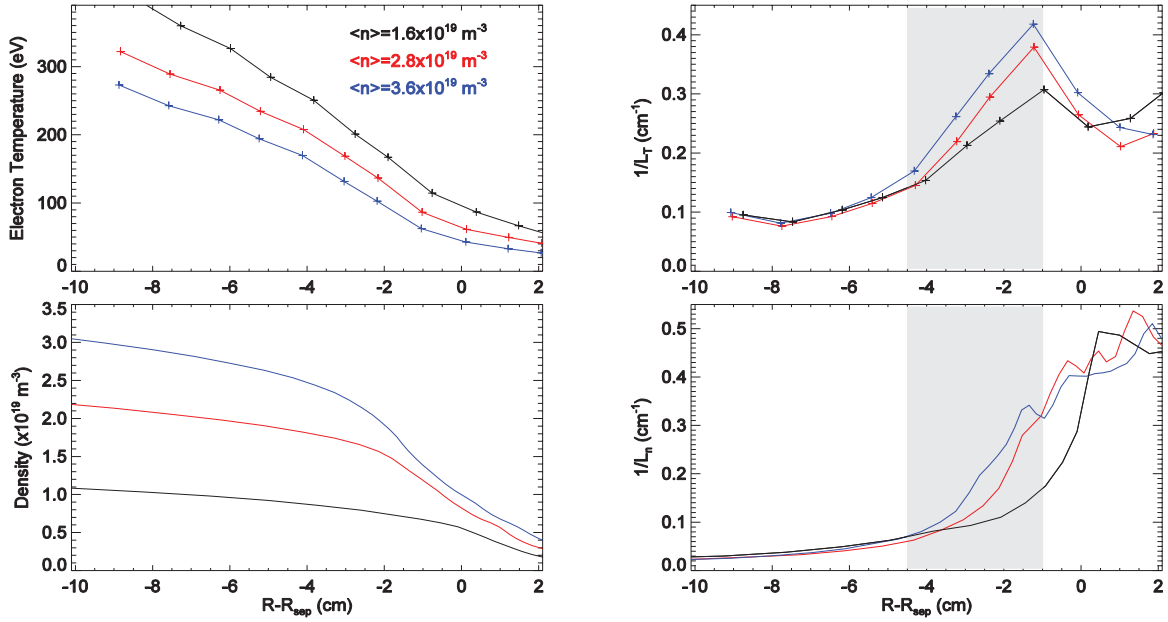

Figure 13. Density and temperature radial profiles (left) and the respective inverse scale-length (right) for different discharge densities at same I_p for discharge #87802. The shaded area indicates the GAM existence regions.

As mentioned before, a linear relationship between the scattered power and the fluctuation level is expected at low turbulence levels. However, when the turbulence level increases, multiple scattering of the probing beam can occur and the relationship between the turbulence level and the scattered power could be no longer linear [51]. As a consequence, the density fluctuation level inferred from the scattered wave amplitude may be underestimated for high turbulence levels. The fact that changes are seen in our density fluctuation measurements is evidence that the signal is not completely saturated. However, it could be the case that the regime is being approached and observe changes in amplitude are smaller than actual changes.

6. Isotope effect

The impact of isotope mass on the GAM amplitude has also been investigated on JET comparing hydrogen and deuterium plasmas. DBS data is available from a few deuterium pulses that also used the VT configuration. The dependence of the GAM amplitude on the plasma line-averaged density for hydrogen and deuterium plasmas at $I_p = 2.5$ MA is shown in figure 14. Results indicate that the GAM amplitude is larger for deuterium plasmas (by about 20% at $\langle n \rangle \approx 2.8 \times 10^{19}\,\mathrm{m}^{-3}$) in agreement with previous findings in TEXTOR [39], FT-2 [40] and AUG [41] suggesting the importance of multi-scale physics for unravelling the physics of the isotope effect in fusion plasmas. Interestingly, on the TJ-II stellarator the amplitude of the ZFs was found to decrease slightly with D/H ratio, in contrast to findings in tokamak plasmas [52]. The limited dataset available to date on JET and the complex dependence of the GAM amplitude on plasma parameters prevents a more definitive conclusion.

We have shown in the previous section that the GAM amplitude depends on the edge plasma electron pressure. It is therefore relevant to evaluate if the larger GAM amplitude observed in deuterium plasmas is associated with a higher edge electron pressure. Figure 15 shows the density and temperature equilibrium profiles for similar discharges in

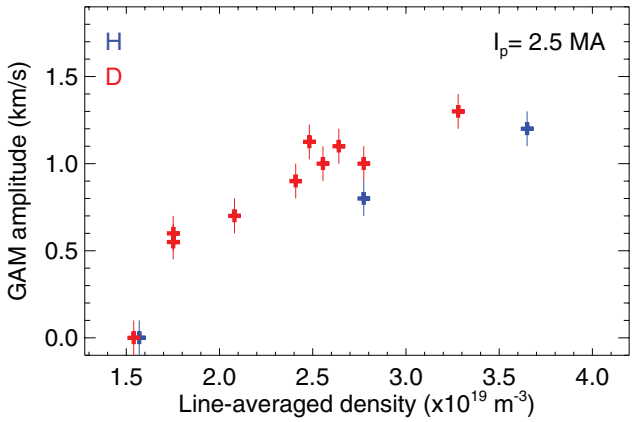

Figure 14. Dependence of the GAM amplitude on the plasma density for hydrogen and deuterium plasmas at $I_p = 2.5$ MA.

hydrogen (#87802) and deuterium (#88871). Note that the line-averaged density is roughly 5% higher for the hydrogen discharge. Taking into account this difference in the line-averaged density and the typical uncertainties associated with the separatrix position we conclude that the higher GAM amplitude in deuterium plasmas cannot be attributed to the edge electron pressure.

Summary and conclusions

GAMs have been investigated in the JET edge plasma for ohmic discharges using mainly DBS. Characteristics and scaling properties of the GAM have been studied. Radially-resolved measurements indicate that GAMs are located in a narrow layer at the edge density gradient region with amplitude up to ~1.5 km s^{-1} corresponding to about 50% of the mean local perpendicular velocity. The GAM shearing rate is in the order 1.3×10^5 s^{-1}, that is comparable to that of the mean flow.

The local mean perpendicular velocity is not the most adequate reference to compare with the GAM amplitude as it can be modified by different processes not related to the physics of GAMs. It is therefore relevant to estimate the potential perturbation associated with GAMs, $e\phi_{GAM}/T_e$, that can be determined by $eE_{r,GAM}/k_r T_e$. For the analyzed ohmic discharges, the GAM potential perturbation is estimated to be in the order of 5%, which is significant taking for instance as reference the frequency integrated density fluctuations that are typically below 5% near the pedestal top in L-mode (e.g. [53]).

GAMs on JET appear to be regulated by the turbulence drive rather than by their damping rate. Theoretical considerations suggest increasing damping of the GAM at low safety factor, contrary to JET observations. The GAM amplitude is found to depend on the edge pressure gradients suggesting a turbulence drive. Finally, it is shown that for the limited dataset available the GAM amplitude is ~20% larger in deuterium than in hydrogen plasmas.

The present work was limited to ohmic plasmas; however, the importance of GAMs when approaching L–H transition will be investigated in the near future. As GAMs exist in the edge region of the plasma and have a significant shearing rate they may play an important role in the L–H transition process.

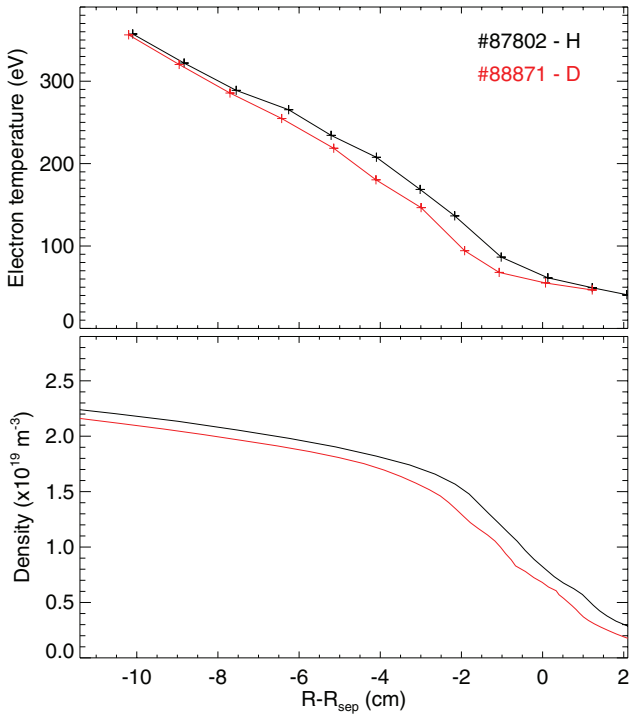

Figure 15. Density and electron temperature equilibrium profiles for similar discharges in hydrogen (#87802) and deuterium plasmas (#88871) at $I_p = 2.5$ MA.

Acknowledgments

This work has been carried out within the framework of the EUROfusion Consortium and has received funding from the Euratom research and training programme 2014–2018 under grant agreement No 633053. IST activities also received financial support from 'Fundação para a Ciência e Tecnologia' through project UID/FIS/50010/2013. The views and opinions expressed herein do not necessarily reflect those of the European Commission.

References

[1] Diamond P.H., Itoh S.-I., Itoh K. and Hahm T.S. 2005 *Plasma Phys. Control. Fusion* **47** R35
[2] Fujisawa A. 2009 *Nucl. Fusion* **49** 013001
[3] Conway G.D. *et al* 2011 *Phys. Rev. Lett.* **106** 065001
[4] Estrada T. *et al* 2011 *Nucl. Fusion* **51** 032001
[5] Winsor N., Johnson J.L. and Dawson J.M. 1968 *Phys. Fluids* **11** 2448
[6] Wahlberg C. 2009 *Plasma Phys. Control. Fusion* **51** 085006
[7] de Meijere C.A. 2014 *Plasma Phys. Control. Fusion* **56** 072001
[8] Angelino P. *et al* 2008 *Phys. Plasmas* **15** 062306
[9] Gao Z. 2011 *Plasma Sci. Technol.* **13** 15
[10] Conway G.D. *et al* 2008 *Plasma Phys. Control. Fusion* **50** 055009
[11] Itoh K., Itoh S., Diamond P.H., Fujisawa A., Yagi M., Watari T., Naga-shima Y. and Fukuyama A. 2006 *J. Plasma Fusion Res.* **1** 037
[12] Gao Z., Itoh K., Sanuki H. and Dong J.Q. 2008 *Phys. Plasmas* **15** 072511
[13] Hillesheim J.C. *et al* 2012 *Phys. Plasmas* **19** 022301
[14] Conway G.D. *et al* 2005 *Plasma Phys. Control. Fusion* **47** 1165

[15] Ido T. *et al* 2006 *Nucl. Fusion* **46** 512
[16] Gurchenko A.D. *et al* 2013 *Plasma Phys. Control. Fusion* **55** 085017
[17] Hamada Y., Nishizawa A., Ido T., Watari T., Kojima M., Kawasumi Y., Narihara K., Toi K. and JIPPT-IIU Group 2005 *Nucl. Fusion* **45** 81
[18] Hamada Y. *et al* 2011 *Nucl. Fusion* **51** 033005
[19] Zonca F. and Chen L. 2008 *Europhys. Lett.* **83** 35001
[20] Zarzoso D. *et al* 2012 *Phys. Plasmas* **19** 022102
[21] Lan T. *et al* 2008 *Plasma Phys. Control. Fusion* **50** 045002
[22] Wang G. *et al* 2013 *Phys. Plasmas* **20** 092501
[23] Silva C., Duarte P., Fernandes H., Figueiredo H., Nedzelskij I., Hidalgo C. and Pedrosa M.A. 2009 *Plasma Phys. Control. Fusion* **51** 085009
[24] Silva C., Arnoux G., Groth M., Hidalgo C. and Marsen S. 2013 *Plasma Phys. Control. Fusion* **55** 025001
[25] Moyer R.A., Tynan G.R., Holland C. and Burin M.J. 2001 *Phys. Rev. Lett.* **87** 135001
[26] McKee G.R. *et al* 2006 *Plasma Phys. Control. Fusion* **48** S123
[27] Zhao K.J. *et al* 2006 *Phys. Rev. Lett.* **96** 255004
[28] Krämer-Flecken A., Soldatov S., Koslowski H.R. and Zimmermann O. 2006 *Phys. Rev. Lett.* **97** 045006
[29] Nagashima Y. *et al* 2005 *Phys. Rev. Lett.* **95** 095002
[30] Xu Y. *et al* 2011 *Nucl. Fusion* **51** 063020
[31] Melnikov A.V. *et al* 2006 *Plasma Phys. Control. Fusion* **48** S87
[32] Zhao K.J. *et al* 2010 *Plasma Phys. Control. Fusion* **52** 124008
[33] Liu A.D., Lan T., Yu C.X., Zhang W., Zhao H.L., Kong D.F., Chang J. F. and Wan B.N. 2010 *Plasma Phys. Control. Fusion* **52** 085004
[34] Fujisawa A. *et al* 2004 *Phys. Rev. Lett.* **93** 165002
[35] Shats M.G., Xia H. and Yokoyama M. 2006 *Plasma Phys. Control. Fusion* **48** S17
[36] Conway G.D. and ASDEX Upgrade Team 2008 *Plasma Phys. Control. Fusion* **50** 085005
[37] Silva C., Hidalgo C., Figueiredo H., Duarte P., Fernandes H., Nedzelskiy I. and Pedrosa M.A. 2008 *Phys. Plasmas* **15** 120703
[38] Yashin A.Yu. *et al* 2014 *Nucl. Fusion* **54** 114015
[39] Xu Y. *et al* 2013 *Phys. Rev. Lett.* **110** 265005
[40] Gurchenko A.D. *et al* 2016 *Plasma Phys. Control. Fusion* **58** 044002
[41] Hennequin P. *et al 42nd European Physical Society Conf. on Plasma Physics (Lisbon, 22–26 June 2015)* I1.102
[42] Hirsch M. *et al* 2001 *Plasma Phys. Control. Fusion* **43** 1641
[43] Sirinelli A. *et al* 2013 *11th Int. Reflectometry Workshop (Paris, April 2013)* http://www.lptp.polytechnique.fr/news/11/Workshop/index.html
[44] Meneses L. *et al* 2011 *Fusion Eng. Des.* **86** 552
[45] Hillesheim J.C. *et al* 2015 *Proc. 12th Int. Reflectometry Workshop—IRW12 (Juelich, May 2015* IRW12*)*
[46] Poli E. *et al* 2001 *Comput. Phys. Commun.* **136** 90
[47] Sirinelli A. *et al* 2010 *Rev. Sci. Instrum.* **81** 10D939
[48] Maggi C.F. *et al* 2014 *Nucl. Fusion* **54** 023007
[49] Hillesheim J.C. *et al* 2016 *Phys. Rev. Lett.* **116** 065002
[50] Hahm T.S. *et al* 1999 *Phys. Plasmas* **6** 922
[51] Gusakov E.Z., Surkov A.V. and Popov A.Yu. 2005 *Plasma Phys. Control. Fusion* **47** 959
[52] Liu B., Pedrosa M.A., van Milligen B.Ph., Hidalgo C., Silva C., Tabarés F.L., Zurro B., McCarthy K.J., Cappa A. and Liniers M. 2015 *Nucl. Fusion* **55** 112002
[53] McKee G.R. *et al* 2009 *Nucl. Fusion* **49** 115016
[54] Romanelli F. *et al* 2015 *Nucl. Fusion* **55** 104001